

# Dust Reverberation Mapping of Z229–15

Amit Kumar Mandal<sup>1,2\*</sup>, Suwendu Rakshit<sup>3,4</sup>, C. S. Stalin<sup>2</sup>, Dominika Wylezalek<sup>5</sup>, Markus Kissler Patig<sup>5</sup>, Ram Sagar<sup>2</sup>, Blesson Mathew<sup>1</sup>, S. Muneer<sup>2</sup>, Indrani Pal<sup>2</sup>

<sup>1</sup>*Department of Physics, CHRIST (Deemed to be University), Hosur Road, Bangalore 560 029, India*

<sup>2</sup>*Indian Institute of Astrophysics, Block II, Koramangala, Bangalore, 560 034, India*

<sup>3</sup>*Aryabhata Research Institute of Observational Sciences, Manora Peak, Nainital 263002, India*

<sup>4</sup>*Finnish Centre for Astronomy with ESO (FINCA), University of Turku, Quantum, Vesilinnantie 5, 20014 University of Turku, Finland*

<sup>5</sup>*European Southern Observatory, Karl-Schwarzschildstr. 2, D-85748 Garching bei München, Germany*

Accepted 08 December 2020. Received 08 December 2020; in original form 14 September 2020

## ABSTRACT

We report results of the dust reverberation mapping (DRM) on the Seyfert 1 galaxy Z229–15 at  $z = 0.0273$ . Quasi-simultaneous photometric observations for a total of 48 epochs were acquired during the period 2017 July to 2018 December in B, V, J, H and  $K_s$  bands. The calculated spectral index ( $\alpha$ ) between B and V bands for each epoch was used to correct for the accretion disk (AD) component present in the infrared light curves. The observed  $\alpha$  ranges between  $-0.99$  and  $1.03$ . Using cross-correlation function analysis we found significant time delays between the optical V and the AD corrected J, H and  $K_s$  light curves. The lags in the rest frame of the source are  $12.52^{+10.00}_{-9.55}$  days (between V and J),  $15.63^{+5.05}_{-5.11}$  days (between V and H) and  $20.36^{+5.82}_{-5.68}$  days (between V and  $K_s$ ). Given the large error bars, these lags are consistent with each other. However, considering the lag between V and  $K_s$  bands to represent the inner edge of the dust torus, the torus in Z229–15 lies at a distance of 0.017 pc from the central ionizing continuum. This is smaller than that expected from the radius luminosity (R–L) relationship known from DRM. Using a constant  $\alpha = 0.1$  to account for the AD component, as is normally done in DRM, the deduced radius (0.025 pc) lies close to the expected R–L relation. However, usage of constant  $\alpha$  in DRM is disfavoured as the  $\alpha$  of the ionizing continuum changes with the flux of the source.

**Key words:** galaxies: active < Galaxies, galaxies: Seyfert < Galaxies, (galaxies:) quasars: individual:... < Galaxies

## 1 INTRODUCTION

Active Galactic Nuclei (AGN) are amongst the most luminous objects ( $10^{42} - 10^{48}$  erg s<sup>-1</sup>) in the Universe and emit energy over all wavelengths. They are believed to be powered by accretion of matter onto super massive black hole (SMBH;  $10^6 - 10^{10}$  M<sub>⊙</sub>) located at the centers of galaxies. The process of accretion forms an accretion disk around the SMBH that radiates predominantly in the ultra-violet (UV) and optical wavelengths (Salpeter 1964; Lynden-Bell 1969; Shakura & Sunyaev 1973). The broad line region (BLR) that lies outside the accretion disk, produces the line emission due

to reprocessing of the UV/optical radiation from the accretion disk. Further out from the BLR is the obscuring torus that is responsible for the thermal infrared emission. Among the different types of AGN are the Seyfert galaxies (Seyfert 1943). Depending on the presence or absence of broad emission lines in their spectra, Seyfert galaxies are divided into Seyfert 1 and Seyfert 2 galaxies. According to the Unified model of AGN, the obscuring torus located within a few parsecs from the central SMBH is responsible for the separation of Seyfert galaxies into Seyfert 1 and Seyfert 2 category (Antonucci 1993; Urry & Padovani 1995). For a typical Seyfert galaxy with a UV luminosity of  $10^{42} - 10^{44}$  erg s<sup>-1</sup>, BLR lies at about  $\sim 0.01$  pc from the accretion disk and the inner edge of the dust torus surrounding the BLR, can extend from 0.01 – 0.1 pc. So, the central regions of AGN are very

\* E-mail: amitkumar@iiap.res.in

compact and not possible to image directly. Therefore, it is difficult to know by direct means the dimension of the BLR and the dust torus in an AGN.

Two methods are currently available to determine the inner extent of the dust torus in an AGN. The first one called reverberation mapping (Blandford & McKee 1982; Peterson 1993) uses the intrinsic characteristic of AGN, namely its flux variability. The optical/UV continuum for an AGN is known to show flux variations on time scales of days to years (Wagner & Witzel 1995). The response of the infrared K band signal to the optical continuum variability is delayed by a time interval  $\delta t$  that characterizes the inner edge of the dust torus as  $R_{\text{torus}} < c \times \delta t$ , where  $c$  is the speed of light. This method of determining the extent of the torus via monitoring observations is called dust reverberation mapping (DRM). This is an expensive method in terms of the observations required, however, insensitive to the distance of the source. Using DRM through optical and near infrared (NIR) K band observations, presently the extent of the torus has been measured for about 40 AGN (Koshida et al. 2014; Pozo Nuñez et al. 2014, 2015; Mandal et al. 2018; Ramolla et al. 2018; Minezaki et al. 2019; Sobrino Figaredo et al. 2020). Also, recently using optical and mid infrared (MIR) observations, Lyu et al. (2019) reported results of torus size for most of the Palomar-Green quasars. The MIR time lags were found to follow the relation  $\Delta t \propto L^{0.5}$ , and the average torus size increased with wavelength. The second method available today to measure the extent of the torus in AGN is via NIR or MIR interferometry. This method has also been successful in measuring the size of the torus in about two dozen AGN (Kishimoto et al. 2009, 2011a; Gravity Collaboration et al. 2020). This method is suitable to only nearby bright AGN, while DRM can be used to measure the torus size in any AGN. However, there are systematic differences in the torus size measured by these two methods. The size measured from interferometric observations are always larger than that found from DRM. Also, the dust torus size from NIR interferometric observations do not follow the relation of  $R_{\text{torus}} \propto L^{0.5}$  (Koshida et al. 2014) known from K band DRM observations, instead the half light radius  $R_{1/2}$  which is used as a representative size of the torus varies as  $R_{1/2} \propto L^{0.21}$  (Kishimoto et al. 2011b). Recently, from DRM observation of 22  $z < 0.6$  quasars Minezaki et al. (2019) found  $R_{\text{torus}} \propto L^{0.424}$ .

In spite of the differences in the torus size obtained from DRM and interferometric observations, the strong correlation between the dust lag and the optical luminosity suggests that AGN can be used as a standard candle (Oknyanskij et al. 1999; Oknyanskij & Horne 2001; Yoshii et al. 2014; Hönig 2014; Hönig & Kishimoto 2017). Hönig & Kishimoto (2017) started a large DRM program, 'VEILS' (VISTA Extragalactic Infrared Legacy Survey) that will observe about 1350 targets in the redshift range of  $0.1 < z < 1.2$  to use dust lag as standard candle to constrain cosmological parameters. However, this program will eventually miss the objects in the local universe, which are important to determine the normalization parameter of the AGN distance moduli (Hönig & Kishimoto 2017). As a complement to the VEILS program, in the nearby Universe, we have started a monitoring project called the REverberation Mapping of Active galactic nuclei Program (REMAP; Mandal et al. 2018, 2019). For this program we are using the 2 m Himalayan Chandra Tele-

scope (HCT) at Hanle, India to carry out observations on a suitably selected sample of eight sources taken from the catalogue of Bentz & Katz (2015) that has spectroscopic lag measurements of the BLR. The results on the first target from the REMAP program, namely H0507+164 was published in Mandal et al. (2018). Here, we present the results of the second source, namely Z229–15, a local Seyfert 1 galaxy with redshift  $z=0.0273$ . Located at  $\alpha_{2000} = 19:05:25.94$  and  $\delta_{2000} = +42:27:39.76$ , Z229–15 has a black hole mass of  $1.00_{-0.24}^{+0.19} \times 10^7 M_{\odot}$  (Barth et al. 2011) and a *Gaia* G band brightness of 16.44 mag. In Section 2, we describe the observation and data reduction processes. The analysis is given in Section 3. In Section 4 we discuss the results of this work followed by the summary in Section 5. For the cosmological parameters, we assumed  $H_0 = 73 \text{ km s}^{-1} \text{ Mpc}^{-1}$ ,  $\Omega_m = 0.27$ , and  $\Omega_{\Lambda} = 0.73$  (Koshida et al. 2014).

## 2 OBSERVATION AND DATA REDUCTION

The photometric observations in the optical B and V bands and the infrared J, H, and  $K_s$  bands were carried out during the period 2017 July to 2018 December for a total of 48 epochs using the Himalayan Chandra Telescope (HCT). Optical observations were carried out using the Himalayan Faint Object Spectrograph and Camera (HFOSC) mounted at the Cassegrain focus of HCT. The camera has a  $2048 \times 4096$  SiTe CCD chip with a gain and readout noise of 1.22 electrons/ADU and 4.8 electrons, respectively. Each pixel of the CCD covers a region of  $0.296''$  in the sky. The observations were carried out in binned mode using only the central  $2048 \times 2048$  region of the CCD, thus covering a field of view of  $10' \times 10'$ . The exposure time in B and V bands is 150 sec and 50 sec, respectively. The NIR observations in the J, H, and  $K_s$  bands were done after the V band observations at each epoch using the TIFR Near Infrared Spectrometer (TIRSPEC) mounted on one of the side ports of HCT (Ninan et al. 2014). The detector used in TIRSPEC is a  $1024 \times 1024$  HgCdTe array with a pixel size of  $18 \mu\text{m}$  covering a field of view of  $5' \times 5'$ . It has a readout noise and gain of 21.5 electrons and 5 electrons/ADU, respectively. The NIR images were taken in 3 dither positions consisting of five exposures each of 20 sec in each of the three NIR filters namely J, H, and  $K_s$ . Sky regions were also observed in the same dithering pattern as the science frames to generate the master sky frame.

### 2.1 Data reduction

The optical data were reduced using IRAF (Image Reduction and Analysis Facility) and MIDAS (Munich Data Analysis System). We followed the standard procedures for image reduction, such as bias subtraction, dark subtraction and flat-fielding. Cosmic rays were removed using MIDAS. The NIR images were reduced using TIRSPEC NIR Data Reduction Pipeline (Ninan et al. 2014). The pipeline produces the final combined images after performing dark subtraction and flat fielding on the raw image frames.

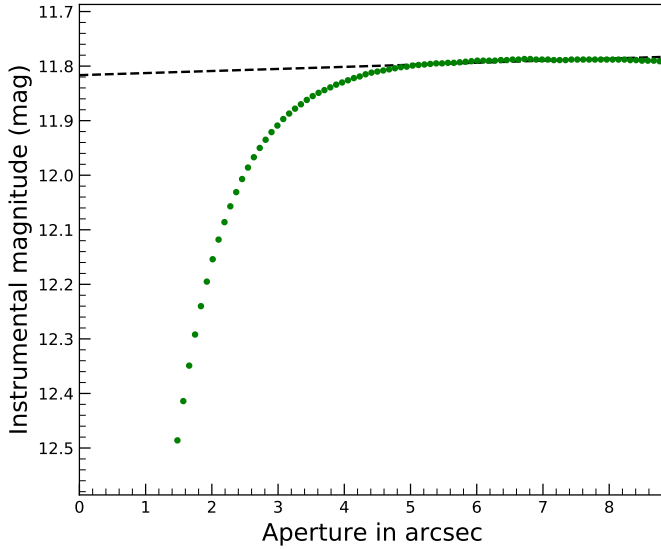


**Figure 1.** Growth curve for a comparison star in V band. The dashed line is the linear least squares fit to the points with aperture sizes between 4 and 6 times the FWHM.

## 2.2 Optical photometry

The objects in the observed image frames were detected using the *daofind* task in IRAF. Photometry of those detected objects were then carried out using the *phot* task in IRAF. Of the detected objects we selected two comparison stars having similar brightness to the AGN to carry out differential photometry and to bring the instrumental magnitude to the standard system. The instrumental magnitudes were obtained in several concentric circular apertures centered on the comparison stars starting from FWHM to about 8 times the FWHM. Growth curves were generated and the final instrumental magnitude for each of the comparison star in an epoch is obtained by the curve of growth (COG) method. This adoption of the COG method ensures that the total flux from a point source is measured. The growth curve for a comparison star is shown in Fig. 1. We fit a straight line using the photometric points between 4 and 6 times the FWHM of the point source (at which point the COG smoothly merges with the background) and the intercept of that line (shown as a dashed line in Fig. 1) was taken as the magnitude of the point source. The two comparison stars that were used to get the correction factors to bring the magnitudes of Z229–15 to the standard system are found to be steady during the duration of our observations. The differential light curve (DLC) of these two stars in the V band are shown in Fig. 2. The DLC has a standard deviation of 0.008 mag, while the mean error of the photometric points in the DLC is 0.004 mag. Given that the photometric errors given by the *phot* task in IRAF is an underestimate by a factor of about 1.75 (Gopal-Krishna et al. 1995), the standard deviation of the DLC of the two stars is consistent with the photometric error, which confirms that the two stars are not variable during the period of our observations.

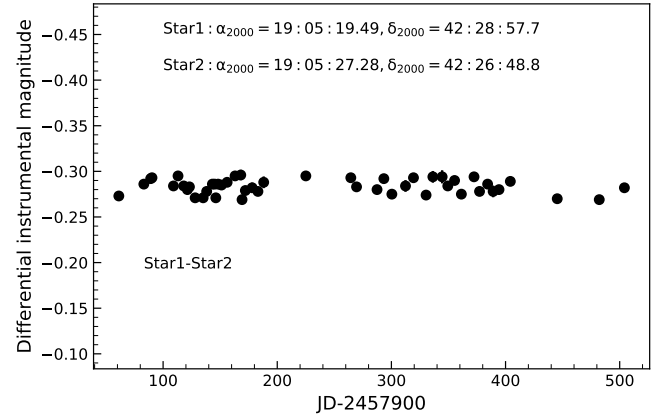


**Figure 2.** Differential light curve of two stars, Star 1 ( $\alpha_{2000} = 19:05:19.49$ ,  $\delta_{2000} = 42:28:57.7$ ) and Star 2 ( $\alpha_{2000} = 19:05:27.28$ ,  $\delta_{2000} = 42:26:48.8$ ) in V band present in the observed field of Z229–15.

## 2.3 Correction for the host-galaxy contribution

The COG method used to obtain the magnitude of the comparison stars could not be used for the target AGN as both the B and V band images have a prominent host galaxy contribution (see Fig. 3 left). The contribution of the host galaxy in both the B and V band needs to be subtracted to get the true flux from the AGN in B and V bands. For that, we used the two dimensional image-decomposition code GALFIT (Peng et al. 2002). For one good epoch of observation in B and V bands, we fitted a Sérsic profile and an edge-on disk profile component to the data. For generating the model PSF we used a point source present close to the target source. An example of the observed image, the modeled galaxy and the residual image that contains the AGN (after subtraction of the model galaxy) for V band are shown in the middle and right panels of Fig. 3. Light curves of the AGN, ideally, can be generated from the photometry of the residual AGN image obtained after GALFIT. However, it is difficult in practice due to the poor signal-to-noise (S/N) ratio in many epochs of data. Therefore, to get the light curve of the AGN devoid of the host galaxy, we followed the following approach. For each epoch of observation, we did aperture photometry of the target Z229–15 at an aperture radius equal to the aperture used for the comparison stars of that epoch. The derived flux ( $F_{\text{total}}$ ) contains the light from the AGN ( $F_{\text{AGN}}$ ) and the host galaxy ( $F_{\text{host}}$ ). Now to remove the host galaxy light we did aperture photometry on the modeled galaxy image (obtained from GALFIT and without the AGN) at different concentric aperture sizes. The flux of the galaxy as a function of radii from its center was generated and then modeled as a polynomial. This is shown in Fig. 4. Once the functional form of the galaxy light distribution was obtained, we found the contribution of galaxy at the radius used for the photometry of Z229–15 for that epoch. This was then subtracted from the total flux to get the light curve of the AGN as

$$F_{\text{AGN}} = F_{\text{total}} - F_{\text{host}} \quad (1)$$

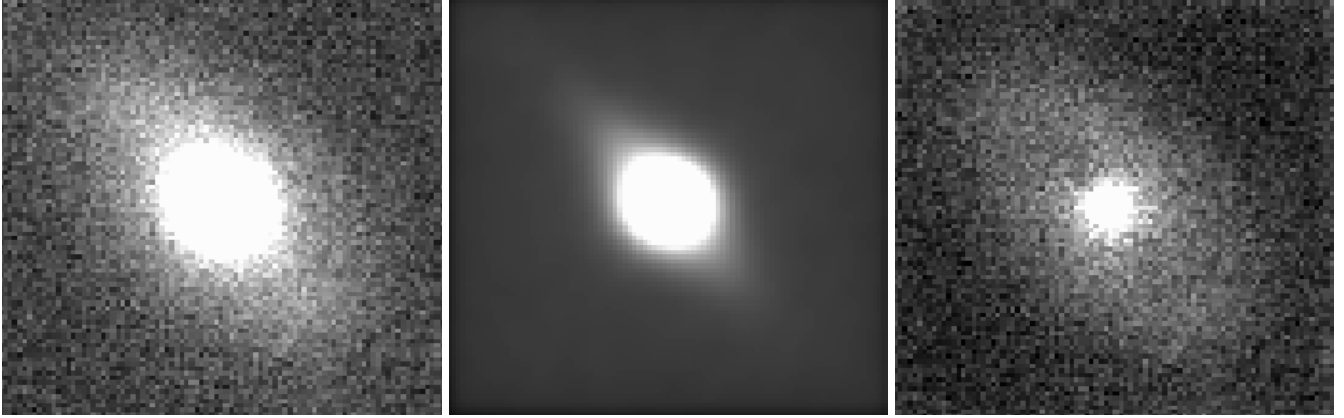


**Figure 3.** Observed V band image of Z229–15 (left). Modeled galaxy image (middle) and residual image containing the AGN at the center (right) obtained from GALFIT.

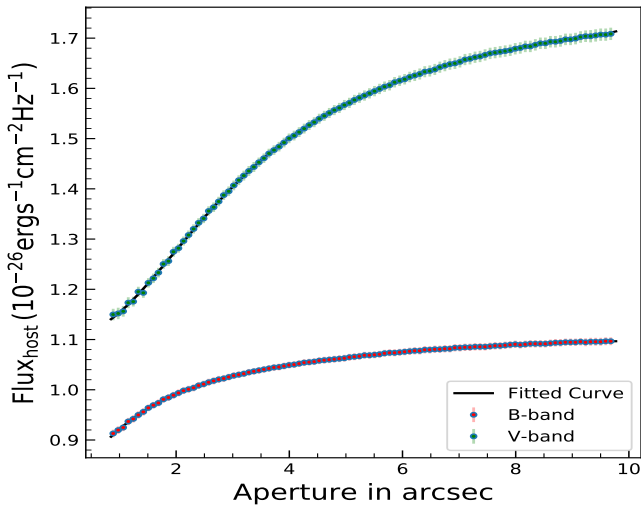


**Figure 4.** Host-galaxy flux as a function of aperture size. The points with error bar are the galaxy-flux values and the solid black lines are the best polynomial fits.

The above was carried out for each epoch of observation to arrive at the final B and V band light curves of the AGN. Finally, the observed instrumental magnitudes were converted into apparent magnitudes using differential photometry relative to the two comparison stars having brightness similar to the AGN in the field, and, whose apparent magnitudes were taken from [Barth et al. \(2011\)](#) and [Fedorov et al. \(2011\)](#) for V and B band, respectively. These comparison stars are found to be non-variable during our monitoring period (see Fig. 2). The obtained apparent magnitudes were corrected for Galactic extinction from the NASA/IPAC Extragalactic data base (NED)<sup>1</sup>. These magnitudes were then converted into fluxes using the zero points taken from [Bessell \(1979\)](#).

<sup>1</sup> <https://nedwww.ipac.caltech.edu>

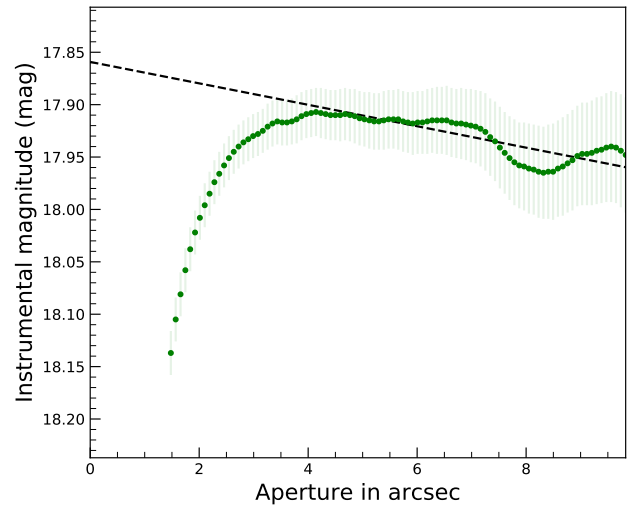


**Figure 5.** Growth curve for a comparison star in  $K_s$  band. The dashed line is the linear least squares fit to the points with aperture sizes between 4 and 6 times the FWHM.

## 2.4 Infrared photometry

The images acquired in the NIR J, H and  $K_s$  bands have very poor S/N compared to the optical B and V band images. Also, the PSF is found to change across the image frames. Similar to the optical band we tried to obtain the magnitude of the comparison star and Z229–15 (as the host galaxy is not seen) using the COG method. However, we found the COG not to smoothly merge with the background and instead showed many wiggles (see Fig. 5). Therefore, to obtain the total fluxes from the comparison stars and the AGN we followed a two step approach. We carried out aperture photometry on a sequence of circular apertures. We calculated S/N at each of the aperture and plotted S/N as a function of aperture to find the aperture at which the S/N is maximum (see Fig. 6, top panel). We used that aperture to find the magnitude of the objects. The aperture at which the S/N is maximum changes from epoch to epoch. Due to poor S/N, the optimum aperture obtained by this method is much smaller than the FWHM and therefore, the flux obtained on

**Table 1.** Results of photometry. The fluxes and their uncertainties in different photometric bands are in units of  $10^{-26}$  erg s $^{-1}$  cm $^{-2}$  Hz $^{-1}$ . JD in days is given as JD – 2457900.00.

JD(B)	F(B)	$\sigma_B$	JD(V)	F(V)	$\sigma_V$	$\alpha$	JD(J)	F(J)	$\sigma_J$	JD(H)	F(H)	$\sigma_H$	JD(K)	F(K)	$\sigma_K$
–	–	–	61.2132	0.475	0.012	–	61.2006	3.437	0.171	61.1952	4.284	0.172	61.1898	4.769	0.263
–	–	–	83.1235	0.577	0.012	–	83.0986	4.514	0.164	83.0931	4.589	0.164	83.0869	5.323	0.214
–	–	–	89.1020	0.499	0.011	–	89.0899	3.436	0.141	89.0846	4.481	0.166	89.0790	4.853	0.208
90.2687	0.589	0.009	90.2637	0.526	0.012	0.508	90.1166	3.548	0.136	90.1111	4.626	0.162	90.1056	4.953	0.203
109.0943	0.775	0.009	109.0821	0.699	0.011	0.467	109.1157	3.635	0.152	109.1104	4.803	0.174	109.1024	5.445	0.237
113.0778	0.629	0.008	113.0743	0.580	0.011	0.361	118.0661	3.752	0.175	118.0606	4.858	0.177	118.0547	5.466	0.233
118.0949	0.674	0.009	118.0811	0.606	0.011	0.478	121.2985	4.258	0.175	121.3043	5.214	0.186	121.3095	6.104	0.248
121.2953	0.681	0.009	121.2823	0.593	0.010	0.623	123.0859	3.678	0.162	123.0921	5.063	0.181	123.0983	5.631	0.235
123.0754	0.676	0.009	123.0688	0.644	0.011	0.219	128.0531	3.952	0.170	128.0531	4.936	0.179	128.0641	6.173	0.252
128.0900	0.716	0.009	128.0763	0.633	0.011	0.556	135.0515	3.920	0.162	135.0656	5.156	0.184	135.0710	6.050	0.249
135.0910	0.641	0.008	135.0858	0.619	0.011	0.155	138.1881	4.195	0.183	138.1940	5.010	0.178	138.1996	5.955	0.243
138.1768	0.597	0.008	138.1716	0.557	0.011	0.318	140.0493	3.934	0.171	140.0571	4.970	0.296	143.1466	5.934	0.245
143.1754	0.607	0.008	143.1723	0.546	0.011	0.479	143.1576	4.128	0.168	143.1576	4.885	0.174	145.1724	5.970	0.254
145.1519	0.590	0.008	145.1388	0.557	0.010	0.259	145.1555	4.281	0.182	145.1666	4.745	0.177	146.1533	6.050	0.253
146.1875	0.592	0.008	146.1770	0.567	0.010	0.194	146.1643	4.077	0.176	146.1589	4.979	0.176	148.1671	5.909	0.240
148.1609	0.618	0.008	148.1557	0.599	0.010	0.143	148.1777	4.062	0.164	148.1726	4.941	0.174	151.2010	5.958	0.343
151.1697	0.584	0.008	151.1627	0.577	0.010	0.059	151.1863	4.016	0.381	151.1946	5.389	0.263	156.0789	7.180	0.282
156.1047	0.578	0.009	156.1011	0.511	0.010	0.554	156.0598	4.763	0.205	156.0732	6.332	0.220	168.0090	5.897	0.234
163.0652	0.600	0.009	163.0527	0.554	0.010	0.352	168.0206	3.859	0.167	168.0149	4.665	0.168	169.1878	5.847	0.253
168.0448	0.654	0.008	168.0346	0.595	0.011	0.426	169.1765	3.679	0.166	169.1822	4.835	0.190	172.0439	6.183	0.256
169.1735	0.612	0.008	169.1642	0.583	0.010	0.218	172.0249	4.107	0.193	172.0363	5.099	0.187	178.0571	5.417	0.231
172.0607	0.608	0.009	172.0555	0.532	0.011	0.605	178.0436	3.454	0.155	178.0510	4.695	0.176	183.1151	6.044	0.258
178.0323	0.350	0.008	178.0257	0.387	0.010	-0.449	183.1041	3.685	0.160	183.1096	4.945	0.184	188.1144	5.172	0.245
183.0956	0.452	0.008	183.0766	0.467	0.010	-0.145	188.1011	3.690	0.168	188.1074	4.333	0.172	225.0356	5.360	0.236
188.1374	0.221	0.008	188.1263	0.272	0.010	-0.930	225.0227	3.976	0.184	225.0297	4.753	0.185	264.4761	5.026	0.228
225.0555	0.325	0.008	225.0455	0.328	0.010	-0.046	264.4650	3.678	0.176	264.4708	4.694	0.185	269.4794	5.067	0.244
264.4490	0.489	0.008	264.4438	0.471	0.011	0.171	269.4901	3.613	0.259	269.4849	4.461	0.201	287.4277	5.448	0.235
269.4742	0.506	0.008	269.4643	0.495	0.011	0.100	287.4387	3.655	0.165	287.4332	4.633	0.168	293.3966	5.860	0.253
287.4235	0.577	0.008	287.4170	0.509	0.011	0.557	293.4109	3.807	0.174	293.4053	4.792	0.177	300.3659	5.370	0.232
293.3921	0.640	0.008	293.3789	0.580	0.011	0.440	300.3530	3.543	0.182	300.3603	4.750	0.182	312.3806	5.073	0.215
300.4129	0.540	0.008	300.4077	0.481	0.010	0.514	312.3697	3.557	0.172	312.3751	4.435	0.165	324.3247	4.968	0.233
312.3519	0.482	0.009	312.3450	0.426	0.011	0.556	319.3554	3.363	0.164	319.3516	4.113	0.191	330.4025	4.861	0.212
319.3354	0.357	0.008	319.3393	0.389	0.010	-0.384	324.3136	3.403	0.170	324.3193	4.563	0.176	336.3635	5.038	0.223
330.3760	0.421	0.008	330.3728	0.398	0.010	0.254	330.3907	3.391	0.154	330.3968	4.115	0.158	344.3510	3.362	0.241
336.3370	0.366	0.008	336.3294	0.343	0.010	0.298	336.3527	3.118	0.153	336.3580	3.769	0.148	349.4212	4.696	0.207
344.4617	0.334	0.009	344.4566	0.416	0.011	-0.986	344.4466	2.650	0.181	344.4413	3.014	0.179	355.4278	4.926	0.228
349.4072	0.530	0.008	349.4019	0.478	0.010	0.467	349.4331	3.190	0.160	349.4275	4.105	0.162	361.3132	4.847	0.219
355.3493	0.622	0.008	355.3386	0.573	0.011	0.369	355.4170	3.019	0.159	355.4223	4.091	0.162	377.2408	5.145	0.247
361.2995	0.615	0.008	361.3054	0.550	0.011	0.500	361.3274	3.444	0.169	361.3216	4.319	0.166	384.2644	5.676	0.268
372.3871	0.752	0.009	372.3810	0.598	0.011	1.029	372.3407	3.640	0.164	372.3256	4.780	0.178	389.1509	5.492	0.269
377.2167	0.731	0.009	377.2085	0.659	0.011	0.463	377.2276	3.589	0.177	377.2351	4.322	0.176	394.2799	5.423	0.252
384.3065	0.782	0.009	384.3013	0.702	0.012	0.485	384.2538	3.640	0.187	384.2588	4.672	0.192	404.1516	5.110	0.268
389.1414	0.753	0.010	389.1275	0.712	0.012	0.251	389.1633	3.851	0.196	389.1578	4.972	0.200	445.2798	4.626	0.312
394.2751	0.751	0.010	394.2650	0.647	0.012	0.670	394.2913	3.567	0.177	394.2856	4.681	0.184	482.0729	4.386	0.204
404.1918	0.422	0.008	404.1883	0.440	0.011	-0.190	404.1678	2.890	0.253	404.1572	4.500	0.196	504.1383	6.320	0.269
445.2936	0.131	0.007	445.2905	0.163	0.010	-0.967	445.2718	2.763	0.156	445.2757	3.864	0.167	–	–	–
482.1024	0.701	0.009	482.0976	0.655	0.011	0.311	482.0836	2.986	0.137	482.0782	3.858	0.147	–	–	–
504.1248	0.502	0.008	504.1176	0.488	0.011	0.122	504.1508	3.436	0.150	504.1449	4.819	0.173	–	–	–

the comparison stars and the AGN at the optimum aperture is always an underestimation.

Therefore, to get the true brightness of the comparison stars and the AGN we need to apply aperture correction to offset for the missing flux obtained at smaller apertures. We estimated the aperture correction using a mean differential curve of growth (DCOG) analysis. There are three point sources in the observed image frames in the NIR bands. For each of these stars we calculated the magnitude difference between consecutive apertures, i.e  $\Delta m = m_{i+i} - m_i$ , where  $i$  refers to the aperture radius, and plotted  $\Delta m$  against aper-

ture radii as shown in Fig. 6 (bottom panel). A mean DCOG is then obtained by taking the average of the DCOG obtained for these three stars. A polynomial is fit to the mean DCOG. The difference between the  $\Delta m$  at the FWHM and the  $\Delta m$  at the optimum aperture obtained from the best-fit polynomial was applied as aperture correction to each of the comparison stars and the AGN to get their actual brightness. We note that the pattern of the NIR light curves before and after the correction looks nearly identical, however, there is a minor advantage (though not much significant) in using the correction factor obtained from the DCOG. For

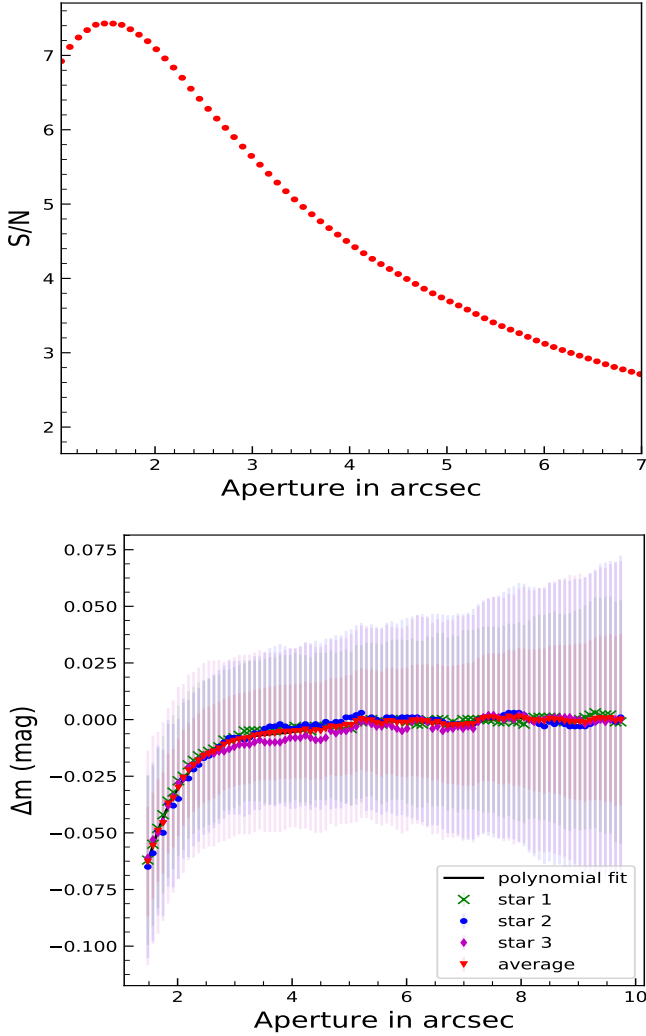


**Figure 6.**  $S/N$  vs. aperture (top). Differential magnitude between successive apertures vs. aperture size (bottom). The green, blue, purple and the red points represent differential magnitudes for comparison star 1, star 2, star 3 and average of those, respectively. The black solid line is the best polynomial fit curve for the average differential magnitudes.

example, the standard deviation of the DLC between Star 1 and Star 2 before applying the correction factor is 0.096 mag in the J band and it reduces to 0.087 mag after applying the correction factors. In the H and  $K_s$  bands, the standard deviation of the DLC between Star 1 and Star 2 are similar before and after application of the correction factors. The final NIR magnitudes were obtained by carrying out differential photometry of the AGN relative to the three comparison stars, the standard magnitudes of which were taken from SIMBAD<sup>2</sup> data base. They were corrected for Galactic extinction using the values taken from NED. Final NIR light curves in flux units were obtained using the zero points from Bessell et al. (1998).

The NIR light curves obtained by the procedure out-

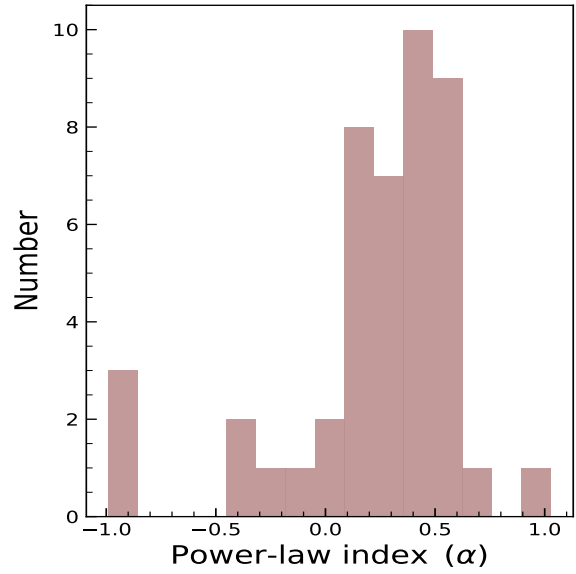


**Figure 7.** Distribution of the spectral index  $\alpha$ .

lined above will have contribution from the torus, the host galaxy, and the infrared emission coming from the accretion disk (AD). The observed infrared radiation can be written as

$$F_{\text{obs}} = F_{\text{dust}} + F_{\text{host}} + F_{\text{AD}} \quad (2)$$

Therefore, to generate the infrared light curves that contain only the reprocessed optical continuum from the accretion disk by the dust torus ( $F_{\text{dust}}$ ), we need to subtract the contribution to the NIR from the host galaxy ( $F_{\text{host}}$ ) and the AD ( $F_{\text{AD}}$ ). However, as the infrared images have poor  $S/N$  and as the AGN is only visible in the NIR images, we did not attempt to correct for  $F_{\text{host}}$  and instead aimed to correct only for the contribution of  $F_{\text{AD}}$  to the observed NIR emission.

## 2.5 Subtraction of the AD component of the NIR flux

The observed NIR emission has contribution from the AD. (Tomita et al. 2006; Kishimoto et al. 2008; Lira et al. 2011). This AD contamination to the NIR fluxes makes the derived lag between the optical and NIR continuum shorter than the actual lag (Koshida et al. 2014). So to get the actual time lag, between the optical and NIR flux variations, the contribution of the AD to the observed NIR fluxes needs to be removed. We estimated the AD contribution to the NIR fluxes by considering a power-law spectrum of the AD (Koshida et al. 2014) and written as

$$f_{\text{NIR}}^{\text{AD}}(t) = f_V(t) \left( \frac{\nu_{\text{NIR}}}{\nu_V} \right)^\alpha \quad (3)$$

where  $f_{\text{NIR}}^{\text{AD}}(t)$  and  $f_V(t)$  represent the accretion disk component of the NIR flux and the V band flux at time  $t$ ,  $\nu_V$  and  $\nu_{\text{NIR}}$  are the effective frequencies of V and the NIR (J, H,  $K_s$ ) bands, respectively, and  $\alpha$  is the power-law index.

AGN do show spectral variations with their brightness (Meusinger et al. 2011). They are known to show a bluer

<sup>2</sup> <http://simbad.u-strasbg.fr/simbad/>

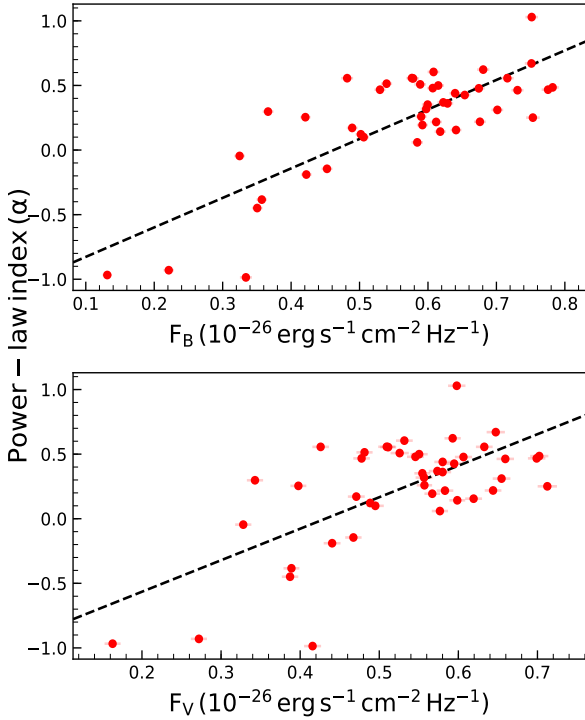


Figure 8. Dependency of  $\alpha$  on B (top) and V band (bottom) flux.

when brighter behaviour (Kokubo et al. 2014) which suggests that AGN have a time dependent power-law index  $\alpha$ . Therefore, each epoch of NIR observation has to be corrected for the AD emission component using the  $\alpha$  evaluated for each epoch. At any given epoch, the observations in the optical and each of the NIR bands were typically obtained within 300 sec of one another, and therefore, they were considered as nearly simultaneous to remove the contribution of AD to each of the NIR bands. We estimated  $\alpha$  for each epoch of observation using the near-simultaneous observations in the optical B and V bands making use of the relation given below (Mandal et al. 2019)

$$\alpha = \frac{\ln(f_B/f_V)}{\ln(\nu_B/\nu_V)} \quad (4)$$

where,  $f_B$  and  $f_V$  are the flux densities in B and V band, respectively, while  $\nu_B$  and  $\nu_V$  are the frequencies in B and V band. The distribution of  $\alpha$  obtained between B and V bands for all the epochs of observations is shown in Fig. 7. The estimated values of  $\alpha$  range between  $-0.99$  and  $1.03$ . We found a median  $\alpha$  of  $0.318$  with a standard deviation of  $0.418$ . This is similar to the value of  $\alpha = 1/3$  expected in the standard accretion model (Shakura & Sunyaev 1973).

The variation of  $\alpha$  with both the B and V band brightness of the source is shown in Fig. 8. We found  $\alpha$  to be correlated significantly with the B and V band brightness with a bluer when brighter trend. Linear least squares fit to the data gave Spearman rank correlation coefficients of  $0.598$  and  $0.442$  with the probability (p) of no correlation of  $10^{-5}$  and  $0.002$  for B and V bands, respectively. The  $\alpha$  value obtained for each epoch was used to calculate the epoch-wise values of  $F_{AD}$  using Equation 3. The calculated values of

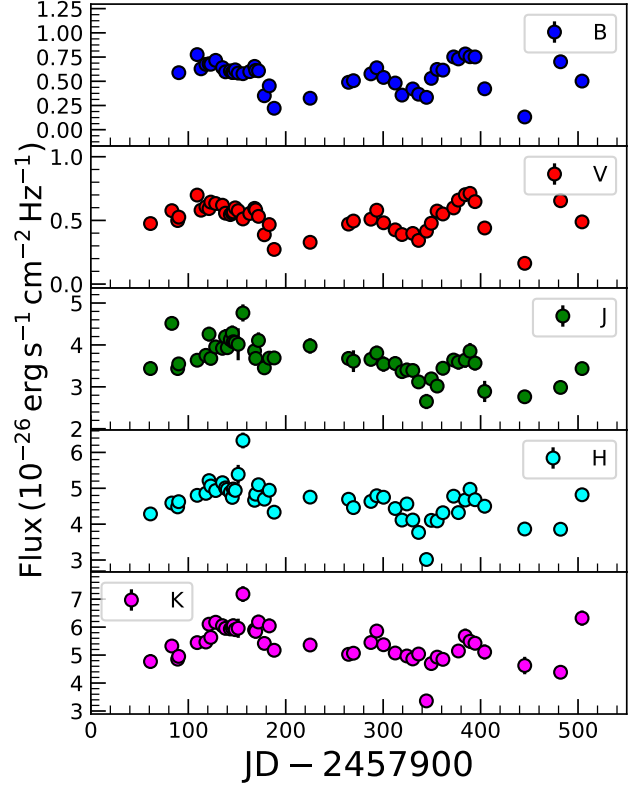


Figure 9. The light curves of Z229–15 in optical B, V and NIR J, H,  $K_s$  bands for the period from 2017 July to 2018 December. The accretion disk component was subtracted from all the NIR light curves using  $\alpha$  measured at individual epoch.

$F_{AD}$  were then subtracted from the observed  $F_{obs}$  values to get the dust contribution. The error in the flux values in the different bands were obtained via error propagation. The results of the photometry are given in Table 1.

### 3 ANALYSIS

#### 3.1 Flux variability

We show in Fig. 9 the final light curves of Z229–15 in the optical B and V bands and the NIR J, H and  $K_s$  bands. We characterised the flux variability of the source using normalized excess variance ( $F_{var}$ ; Edelson et al. 2002; Vaughan et al. 2003; Rani et al. 2017). The uncertainties in the  $F_{var}$  values were calculated following Edelson et al. (2002). The results of the flux variability analysis of the source are given in Table 2. Here,  $\langle f \rangle$  and  $\sigma$  are the mean and standard deviation of the light curves and  $R_{max}$  is the ratio between the maximum and minimum flux in the light curve. We found wavelength dependent variability with the amplitude of variability in the shorter wavelength (B band) larger than that at the longer wavelength ( $K$  band).

#### 3.2 Lag between optical and NIR variations

The light curves in the optical B, V and the NIR J, H,  $K_s$  bands (see Fig. 9) and the results given in Table 1 indicate

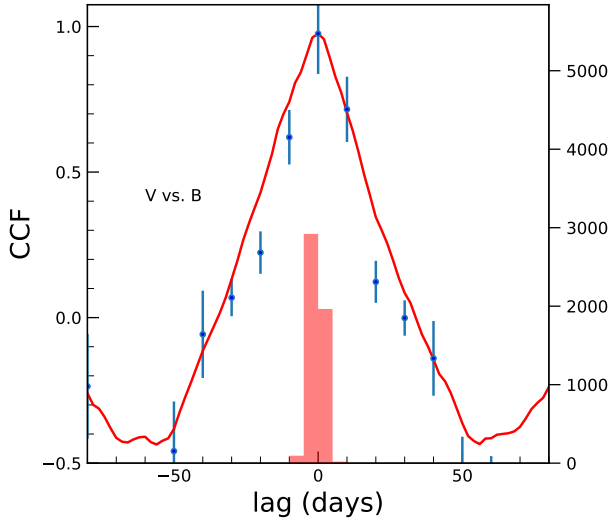


**Figure 10.** Correlation between V and B band. The solid red line represents the ICCF and points with error bars show the DCF. The distribution of  $\tau_{\text{cent}}$  obtained from ICCF is also shown.

**Table 2.** Results of the analysis of variability in the observer’s frame. The mean values of fluxes ( $\langle f \rangle$ ) in various bands and their associated standard deviations  $\sigma$  are in units of  $10^{-26} \text{ erg s}^{-1} \text{ cm}^{-2} \text{ Hz}^{-1}$ .  $\lambda_{\text{eff}}$  is the effective wavelength in Angstroms.

Filter	$\lambda_{\text{eff}}$	$\langle f \rangle$	$\sigma$	$F_{\text{var}}$	$R_{\text{max}}$
B	4363	0.56	0.15	$0.263 \pm 0.000$	5.953
V	5448	0.53	0.11	$0.213 \pm 0.000$	4.374
J	12200	3.66	0.43	$0.106 \pm 0.002$	1.797
H	16300	4.64	0.50	$0.100 \pm 0.002$	2.101
$K_s$	21900	5.46	0.61	$0.102 \pm 0.002$	1.905

that Z229–15 is variable in the optical and NIR bands and therefore it is possible to estimate time lag if any between the flux variation in different optical and NIR bands.

### 3.2.1 Cross-correlation analysis

To estimate the time lag between the optical and the NIR flux variations, we used two well known cross correlation function (CCF) methods, namely the interpolated cross-correlation function (ICCF; Gaskell & Sparke 1986; Gaskell & Peterson 1987) and the discrete correlation function (DCF; Edelson & Krolik 1988). For CCF analysis we used a time bin ( $\tau$ ) of 5 days, as this is the typical sampling of our multi-band light curves. We show in Fig. 10 the DCF (blue filled circles) and ICCF (red solid line) obtained between the optical B and V bands. The CCF peaks at zero lag. Similarly, the CCF for three other filter combinations, namely V/J, V/H and V/ $K_s$  bands calculated using both the ICCF and DCF methods, are shown in Fig. 11. The CCFs peak at a lag different from zero, and also, the pattern of the CCFs obtained by both the DCF and ICCF methods are similar. To estimate the lag from the cross-correlation func-

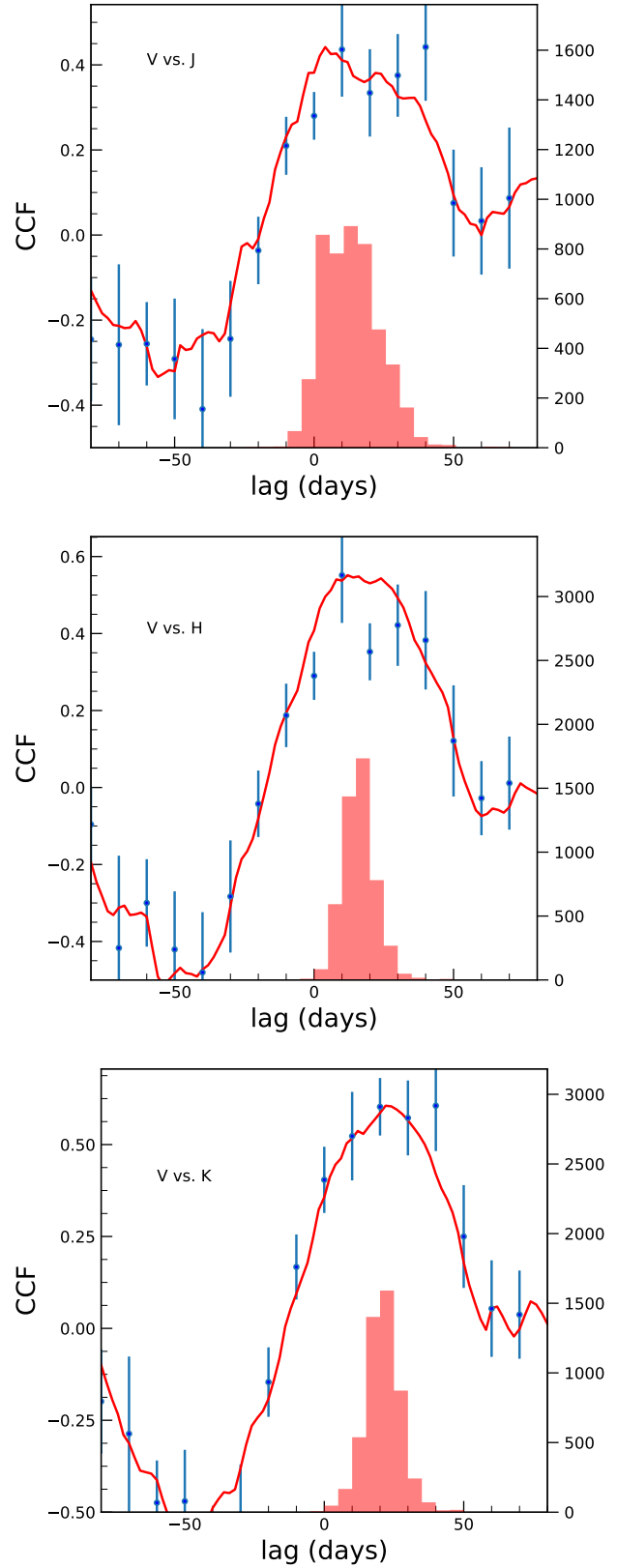


**Figure 11.** The CCFs of V versus J (top panel), V versus H (middle panel), and V versus  $K_s$  (bottom panel) are shown. The solid red line represents the ICCF and the points with error bars show the DCF. The distribution of  $\tau_{\text{cent}}$  obtained from ICCF method

is also shown in each panel.

tion we calculated the centroid  $\tau_{\text{cent}}$  of the CCF as (Peterson et al. 1998)

$$\tau_{\text{cent}} = \frac{\sum_i \tau_i \text{CCF}_i}{\sum_i \text{CCF}_i} \quad (5)$$

For calculating  $\tau_{\text{cent}}$ , we used all the points that are within 80% of the maximum of the CCF. To estimate the uncertainties in the calculated  $\tau_{\text{cent}}$ , we used a model independent Monte Carlo simulation based on flux randomization (FR) and random subset selection (RSS; Peterson et al. 1998; Wandel et al. 1999; Peterson et al. 2004). This was repeated for 5000 times and the centroid of the lag was determined each time. The cross-correlation centroid distribution (CCCD) and cross-correlation peak distribution (CCPD) were then constructed. The CCCDs obtained using the ICCF method are shown in Fig. 10 and Fig. 11. As the CCCD is not Gaussian, the lag is taken as the median of the distribution and the lower and upper error in the lag are that values at the 15.9 and 84.1 percentile of the distribution. This corresponds to 1 sigma error in the case of a Gaussian distribution. The results of the CCF analysis are given in Table 3. The centroid lags calculated using both ICCF and DCF are found to be consistent with each other within error bars. However, in all further analysis we consider the CCCD lags obtained from ICCF method as it has comparatively smaller uncertainties than the DCF lag (see Table 3).

The rest frame time lags corrected for the redshift can be obtained by dividing the observed time lag by a factor of  $(1+z)$  as prescribed by Koshida et al. (2014). Between V and  $K_s$  we obtained a rest frame time lag of  $20.36_{-5.68}^{+5.82}$  days, while between V and H and V and J, we found rest frame time lags of  $15.63_{-5.11}^{+5.05}$  days and  $12.52_{-9.55}^{+10.00}$  days, respectively. There is an indication that the lag obtained between V and  $K_s$  band is larger than V and H, which is larger than V and J. However the error bars are too large to unambiguously argue for the presence of wavelength dependent lag. From these observations, the lags obtained between different wavelengths are consistent with each other. As the inner radius of the dust torus is defined by the lag between V and  $K_s$  band which corresponds to the dust sublimation radius, we used the rest frame lag between V and  $K_s$  band of  $20.36_{-5.68}^{+5.82}$  days to infer the inner edge of the dust torus in Z229–15, which is at a distance of 0.017 pc from the central continuum source.

### 3.2.2 JAVELIN

To calculate the time delays between the optical and different NIR (J, H,  $K_s$ ) bands, we also used the JAVELIN code, developed by Zu et al. (2011, 2013). The driving continuum light curve was modeled using a damped random walk (DRW) process (e.g., Kelly et al. 2009) with two model parameters; amplitude and time scale of variability. A top-hat response function was convolved with the driving continuum light curve to generate the NIR continuum light curve. Therefore, the NIR light curves were the shifted, scaled, and smoothed version of the driving continuum light curve. The Markov chain Monte Carlo (MCMC) approach was used to find the best-fit model maximizing the likelihood. To calculate dust lag, we fitted one optical (V band) and all NIR (J,

**Table 3.** Median values of time delays with errors in days from the CCCDs obtained using DCF and ICCF, CCPD from ICCF and JAVELIN in the observer’s frame.

Band	DCF	ICCF	CCPD from ICCF	JAVELIN
varying $\alpha$				
V – B	$-0.24_{-4.39}^{+3.90}$	$-0.87_{-2.00}^{+1.94}$	$0.00_{-2.00}^{+0.00}$	$-0.57_{-1.29}^{+1.03}$
V – J	$22.33_{-15.16}^{+16.58}$	$12.86_{-9.81}^{+10.27}$	$10.00_{-8.00}^{+14.00}$	$23.82_{-0.45}^{+0.87}$
V – H	$18.16_{-9.91}^{+14.55}$	$16.06_{-5.25}^{+5.19}$	$14.00_{-6.00}^{+12.00}$	$23.28_{-0.40}^{+0.60}$
V – $K_s$	$25.42_{-14.88}^{+13.49}$	$20.92_{-5.84}^{+5.98}$	$22.00_{-10.00}^{+6.00}$	$23.04_{-0.44}^{+0.74}$
constant $\alpha = 0.1$				
V – J	$34.01_{-14.79}^{+11.99}$	$27.96_{-8.73}^{+7.07}$	$28.00_{-8.00}^{+8.00}$	$27.81_{-1.47}^{+1.68}$
V – H	$29.67_{-12.19}^{+11.07}$	$26.14_{-5.12}^{+5.85}$	$26.00_{-4.00}^{+6.00}$	$25.07_{-0.80}^{+1.96}$
V – $K_s$	$34.80_{-12.93}^{+8.69}$	$30.86_{-4.95}^{+6.22}$	$30.00_{-4.00}^{+8.00}$	$24.19_{-0.72}^{+1.92}$

H,  $K_s$  bands) light curves, simultaneously. The best-fit light curve and the probability distribution of the time delay are shown in Fig. 12 for V band and NIR light curves. JAVELIN lag distribution shows two peaks, a significant peak at  $\sim 23$  days and a small peak at  $\sim 29$  days. Considering the overall distribution, we calculated the lags and their uncertainties, which are given in Table 3 in the observer’s frame. We do not find any wavelength-dependent lag from JAVELIN. Almost similar lags between V and NIR bands are found from JAVELIN.

## 4 DISCUSSION

The lag obtained between the optical V band and the NIR  $K_s$  band is believed to represent the inner edge of the dust torus as the temperature of the dust at the wavelength of  $K_s$  band is close to the dust sublimation temperature (Almeida et al. 2017). DRM observations through monitoring in the optical V band and NIR  $K_s$  band have enabled determination of the radius of the inner edge of the torus in about 40 AGN. A majority of those measurements are from the Multicolor Active Galactic Nuclei Monitoring (MAGNUM) project that includes 17 Seyfert 1 galaxies (Koshida et al. 2014) and 22 quasars (Minezaki et al. 2019) and a few objects are from other campaigns (Poza Nuñez et al. 2014, 2015; Ramolla et al. 2018; Mandal et al. 2018).

### 4.1 Infrared lag and optical luminosity correlation

According to Barvainis (1987), the size of the torus is expected to be correlated with the luminosity of the accretion disk as  $R_{\text{torus}} \propto L^{0.5}$ . We show in Fig. 13 the plot of  $R_{\text{torus}}$  determined from K band DRM lags and taken from literature (Koshida et al. 2014; Mandal et al. 2018; Minezaki et al. 2019) against their optical luminosity. In the same figure we show in dotted black line the linear regression relation of  $R_{\text{torus}} \propto L^{0.424}$  (Minezaki et al. 2019) and  $R_{\text{torus}} \propto L^{0.5}$  (Koshida et al. 2014) by dotted red line. The source Z229–15 studied in this work for DRM is shown as a filled red circle in the Figure. Our lag measurement on the Z229–15 deviates from the linear regression line obtained by Minezaki et al. (2019). This deviation could be due to the adoption of variable  $\alpha$  in this work to correct for the contribution of the

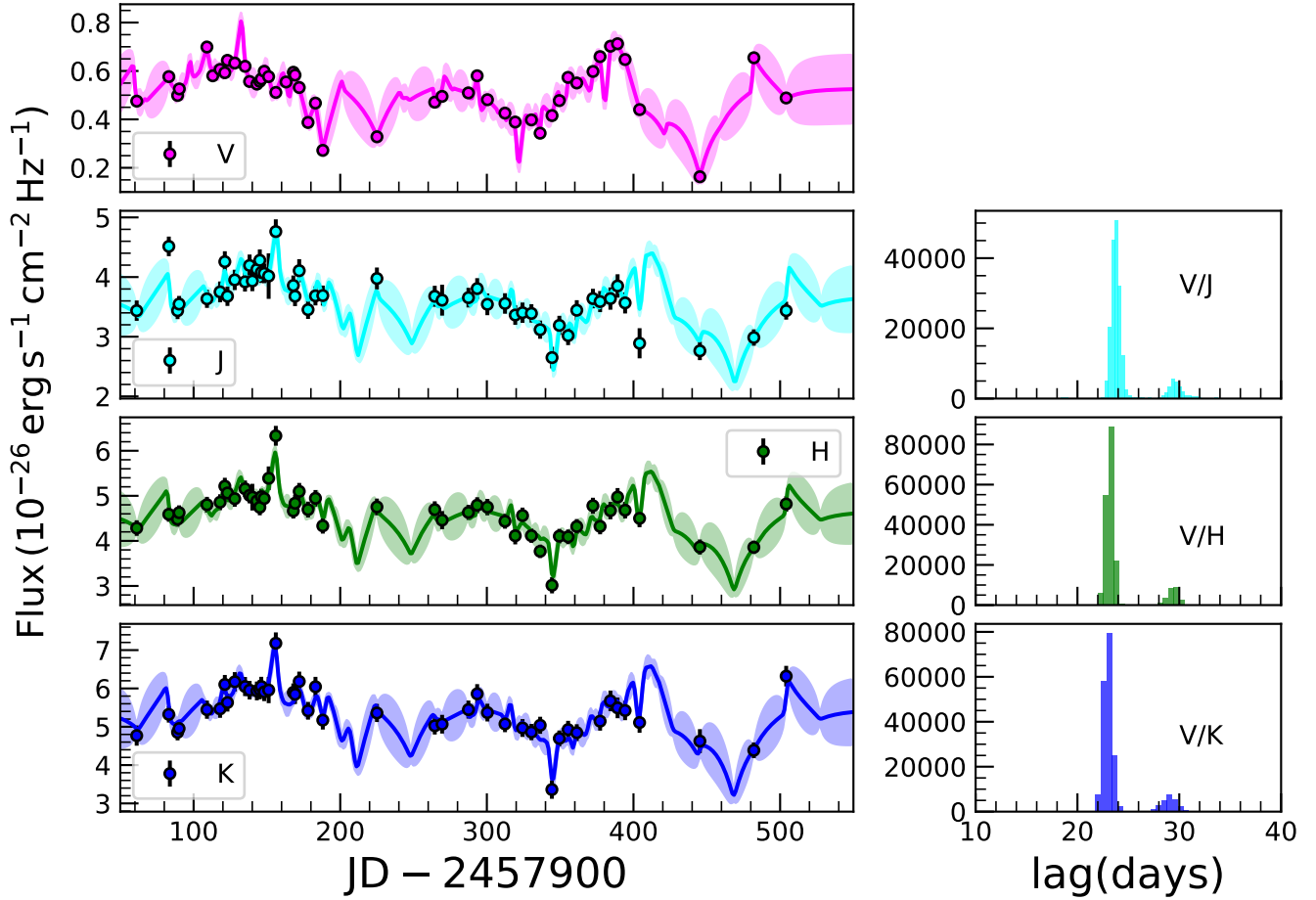


**Figure 12.** Points with error-bars represent observed light curves, whereas the solid lines with shade are the recovered light curves using JAVELIN. The accretion disk contamination in all the NIR light curves was subtracted using  $\alpha$  measured at individual epoch. The histograms represent the probability distribution of the time delay. All the light curves are fitted simultaneously.

AD to the observed NIR light curves. We used  $\alpha$  that was determined for each epoch using the near simultaneous observations in B and V band, while for the lags obtained for the sources in Fig. 13, the authors have used a constant  $\alpha$  to correct for the contribution of the AD to the NIR fluxes. According to Kishimoto et al. (2008) the power law continuum from quasar accretion disk can extend up to NIR with a shape characterised as  $F_\nu \propto \nu^{1/3}$ . AGN are known to show variations in the optical and NIR bands, but the amplitude of flux variations need not be the same across wavelengths. Thus, in addition to flux variations, AGN are also known to show spectral variation (Tomita et al. 2006; Kishimoto et al. 2008). Therefore, it might not be proper to assume a constant  $\alpha$  from optical through NIR to correct for the IR contribution from the AD to the observed IR emission. Despite that, we redid the analysis by adopting a constant  $\alpha$  of 0.1 as used by Minezaki et al. (2019). By this, we obtained a lag between V and K<sub>s</sub> band of  $30.04^{+6.05}_{-4.82}$  days in the rest frame of the source as shown by the red square point which lies closer to the linear regression lines of Koshida et al. (2014) and Minezaki et al. (2019) in Fig. 13. This lag of  $30.04^{+6.05}_{-4.82}$  days corresponds to a distance of 0.025 pc.

From Fig. 13,  $R_{\text{torus}}$  is found to be related to the lumi-

nosity with an index of about 0.5 (ie.  $R_{\text{torus}} \propto L^{0.5}$ ), however, there is scatter. The scatter in the  $R_{\text{torus}} - L$  relation could come from various factors (cf. Minezaki et al. 2019), such as (a) assumption of a constant  $\alpha$  on the removal of the AD component in the observed NIR light curves, (b) effect of viewing angle on the estimated lag (Kawaguchi & Mori 2011; Barvainis 1992), (c) the effect of accretion rate on the measured lag and (d) the distribution of the dust and how it is illuminated by the central source (Almeida et al. 2020). Koshida et al. (2014), by analysing the residuals of the dust lag from the best fit linear regression could not find systematic changes in the dust lag either with the viewing angle or with the accretion rate. Reverberation studies aimed in getting the size of BLR ( $R_{\text{BLR}}$ ) too found a linear correlation between the radius of the BLR and the luminosity with a power law index close to 0.5. However, recently from an analysis of the light curves obtained for the SEAMBH program, Du et al. (2016) found systematically lower BLR size for systems with high accretion rate. They found a slope  $R_{\text{BLR}} \propto L^{0.33}$ , much shallower than the slope of 0.533 found by Grier et al. (2013). Given this observational finding, it is likely that accretion rate in an AGN will also have an influence on the derived dust reverberation lag. Homogeneous

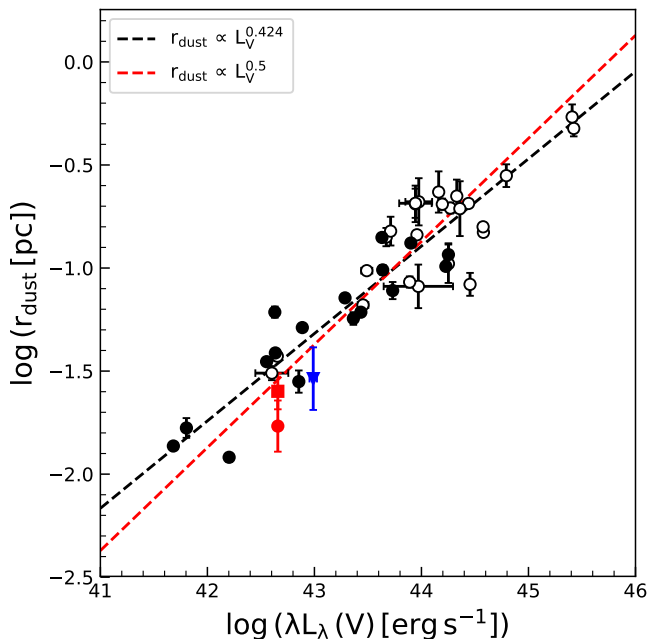


**Figure 13.** Lag – luminosity plot. The lags are in the rest frame of the sources. The empty and filled black circles represent the objects from Minezaki et al. (2019) and Koshida et al. (2014), respectively, triangular blue point represents H0507+164 obtained by Mandal et al. (2018), the red circle and square points correspond to the lag of Z229–15 for  $\alpha$  obtained from observations and a constant  $\alpha = 0.1$ , respectively, in the lag-luminosity plane.

analysis on a larger number of quasars are needed to arrive at a conclusion on the correlation between  $R_{\text{torus}}$  and accretion rate.

#### 4.2 Size of the BLR and the dust torus

Kokubo & Minezaki (2020) by comparing the lag of the  $H\beta$  and the dust torus relative to the optical continuum for the sources in Koshida et al. (2014) found that the dust lags are larger than the  $H\beta$  lag by a factor of about 4 ( $R_{\text{torus}} \sim 4 \times R_{\text{BLR}}$ ). According to Koshida et al. (2014) the dust lag is about five times larger than the BLR lag. In Z229–15 the lag between the optical continuum and the  $H\beta$  emission line from spectroscopic reverberation observations is found to be  $3.86^{+0.69}_{-0.90}$  days in the rest frame of the object (Barth et al. 2011). For Z229–15, the dust lag obtained in this work is about a factor of 5.3 times larger than the BLR lag. This suggests that the BLR lies well inside the dust torus as expected in the Unification model of AGN. There is a hint for wavelength dependent dust lags in our observations, however, due to the larger error bars in the lag between different wavelengths, the presence of wavelength dependent lag in Z229–15 cannot be unambiguously established. Sensitive, long term and high cadence observations of Z229–15 are needed to confirm the presence of wavelength dependent lag if any.

## 5 SUMMARY

We carried out DRM observations of the source Z229–15 in the optical (B, V) and NIR (J, H,  $K_s$ ) bands. We collected near simultaneous photometric data for a total of 48 epochs during the period 2017 July – 2018 December. The results of this work are summarized below:

(i) The host galaxy is prominently seen in the observed B and V band images. We devised a procedure to remove the contribution of the host galaxy to the observed optical light curves and get pure light curves of the optical continuum source.

(ii) The observed NIR light curves do have contribution from the accretion disk. We removed this contribution by using the spectral index obtained between B and V bands for each epoch.

(iii) The host galaxy corrected optical light curves and the accretion disk component corrected NIR light curves show correlated variations among themselves.

(iv) Using cross correlation function analysis we found a rest-frame lag between V and J band of  $12.52^{+10.00}_{-9.55}$  days. Similarly the lags between (V-H) and (V-K) are  $15.63^{+5.05}_{-5.11}$  days and  $20.36^{+5.82}_{-5.68}$  days, respectively. Due to the large error bars the presence of wavelength dependent lags if any could not be ascertained, instead the lag between different wavelengths are consistent with each other.

(v) Considering the lag between V and  $K_s$  to represent the inner edge of the dust torus, we found that the inner edge of the dust torus in Z229–15 is at a distance of 0.017 pc from the central optical ionizing source.

(vi) The dust lag of 20.36 days is about a factor of 5.3 times larger than the BLR lag. This is similar to that known for other AGN.

(vii) Positioning our source in the  $R_{\text{torus}} - L$  relation known for a sample of about 40 DRM source, we found Z229–15 to lie below the  $R_{\text{torus}} - L$  found from DRM observations. However, using a constant spectral index of 0.1 to correct for the AD component in the NIR light curves, we found Z229–15 to move closer to the known  $R_{\text{torus}} - L$  relation. We disfavour usage of constant  $\alpha$  in DRM studies, as  $\alpha$  is known to change with the brightness of the source.

## ACKNOWLEDGEMENTS

We thank the anonymous referee for her/his critical comments that helped to improve our manuscript. We thank the staff at IAO, Hanle and CREST, Hoskote who helped with the observations from the 2 m HCT. The facilities at IAO and CREST are operated by the Indian Institute of Astrophysics, Bangalore. The funding provided by the Humboldt Foundation, Germany is also thankfully acknowledged. AKM and RS thank the National Academy of Sciences, India (NASI), Prayagraj for funding and Director, IIA for hosting and providing infrastructural support to this project.

## DATA AVAILABILITY

The data underlying this article are available in the article and in its online supplementary material.

## REFERENCES

- Almeyda T., Robinson A., Richmond M., Vazquez B., Nikutta R., 2017, *ApJ*, **843**, 3
- Almeyda T., Robinson A., Richmond M., Nikutta R., McDonough B., 2020, *ApJ*, **891**, 26
- Antonucci R., 1993, *ARA&A*, **31**, 473
- Barth A. J., et al., 2011, *ApJ*, **732**, 121
- Barvainis R., 1987, *ApJ*, **320**, 537
- Barvainis R., 1992, *ApJ*, **400**, 502
- Bentz M. C., Katz S., 2015, *PASP*, **127**, 67
- Bessell M. S., 1979, *PASP*, **91**, 589
- Bessell M. S., Castelli F., Plez B., 1998, *A&A*, **333**, 231
- Blandford R. D., McKee C. F., 1982, *ApJ*, **255**, 419
- Du P., et al., 2016, *ApJ*, **825**, 126
- Edelson R. A., Krolik J. H., 1988, *ApJ*, **333**, 646
- Edelson R., Turner T. J., Pounds K., Vaughan S., Markowitz A., Marshall H., Dobbie P., Warwick R., 2002, *ApJ*, **568**, 610
- Fedorov P. N., Akhmetov V. S., Bobylev V. V., 2011, *MNRAS*, **416**, 403
- Gaskell C. M., Peterson B. M., 1987, *ApJS*, **65**, 1
- Gaskell C. M., Sparke L. S., 1986, *ApJ*, **305**, 175
- Gopal-Krishna Sagar R., Wiita P. J., 1995, *MNRAS*, **274**, 701
- Gravity Collaboration et al., 2020, *A&A*, **635**, A92
- Grier C. J., et al., 2013, *ApJ*, **773**, 90
- Hönig S. F., 2014, *ApJ*, **784**, L4
- Hönig S. F., Kishimoto M., 2017, *ApJ*, **838**, L20
- Kawaguchi T., Mori M., 2011, *ApJ*, **737**, 105
- Kelly B. C., Bechtold J., Siemiginowska A., 2009, *ApJ*, **698**, 895
- Kishimoto M., Antonucci R., Blaes O., Lawrence A., Boisson C., Albrecht M., Leipski C., 2008, *Nature*, **454**, 492
- Kishimoto M., Hönig S. F., Antonucci R., Kotani T., Barvainis R., Tristram K. R. W., Weigelt G., 2009, *A&A*, **507**, L57
- Kishimoto M., Hönig S. F., Antonucci R., Barvainis R., Kotani T., Tristram K. R. W., Weigelt G., Levin K., 2011a, *A&A*, **527**, A121
- Kishimoto M., Hönig S. F., Antonucci R., Millour F., Tristram K. R. W., Weigelt G., 2011b, *A&A*, **536**, A78
- Kokubo M., Minezaki T., 2020, *MNRAS*, **491**, 4615
- Kokubo M., Morokuma T., Minezaki T., Doi M., Kawaguchi T., Sameshima H., Koshida S., 2014, *ApJ*, **783**, 46
- Koshida S., et al., 2014, *ApJ*, **788**, 159
- Lira P., Arévalo P., Uttley P., McHardy I., Breedt E., 2011, *MNRAS*, **415**, 1290
- Lynden-Bell D., 1969, *Nature*, **223**, 690
- Lyu J., Rieke G. H., Smith P. S., 2019, *ApJ*, **886**, 33
- Mandal A. K., et al., 2018, *MNRAS*, **475**, 5330
- Mandal A. K., Rakshit S., Pal I., Stalin C. S., Sagar R., Mathew B., 2019, *Bulletin de la Societe Royale des Sciences de Liege*, **88**, 158
- Meusinger H., Hinze A., de Hoon A., 2011, *A&A*, **525**, A37
- Minezaki T., et al., 2019, *ApJ*, **886**, 150
- Ninan J. P., et al., 2014, *Journal of Astronomical Instrumentation*, **3**, 1450006
- Oknyanskij V. L., Horne K., 2001, in Peterson B. M., Pogge R. W., Polidan R. S., eds, *Astronomical Society of the Pacific Conference Series Vol. 224, Probing the Physics of Active Galactic Nuclei*. p. 149
- Oknyanskij V. L., Lyuty V. M., Taranova O. G., Shenavrin V. I., 1999, *Astronomy Letters*, **25**, 483
- Peng C. Y., Ho L. C., Impey C. D., Rix H.-W., 2002, *AJ*, **124**, 266
- Peterson B. M., 1993, *PASP*, **105**, 247
- Peterson B. M., Wanders I., Horne K., Collier S., Alexander T., Kaspi S., Maoz D., 1998, *PASP*, **110**, 660
- Peterson B. M., et al., 2004, *ApJ*, **613**, 682
- Pozo Nuñez F., et al., 2014, *A&A*, **561**, L8
- Pozo Nuñez F., et al., 2015, *A&A*, **576**, A73
- Ramolla M., et al., 2018, *A&A*, **620**, A137
- Rani P., Stalin C. S., Rakshit S., 2017, *MNRAS*, **466**, 3309
- Salpeter E. E., 1964, *ApJ*, **140**, 796
- Seyfert C. K., 1943, *ApJ*, **97**, 28
- Shakura N. I., Sunyaev R. A., 1973, *A&A*, **500**, 33
- Sobrinho Figaredo C., et al., 2020, *AJ*, **159**, 259
- Tomita H., et al., 2006, *ApJ*, **652**, L13
- Urry C. M., Padovani P., 1995, *PASP*, **107**, 803
- Vaughan S., Edelson R., Warwick R. S., Uttley P., 2003, *MNRAS*, **345**, 1271
- Wagner S. J., Witzel A., 1995, *ARA&A*, **33**, 163
- Wandel A., Peterson B. M., Malkan M. A., 1999, *ApJ*, **526**, 579
- Yoshii Y., Kobayashi Y., Minezaki T., Koshida S., Peterson B. A., 2014, *ApJ*, **784**, L11
- Zu Y., Kochanek C. S., Peterson B. M., 2011, *ApJ*, **735**, 80
- Zu Y., Kochanek C. S., Kozłowski S., Udalski A., 2013, *ApJ*, **765**, 106

This paper has been typeset from a  $\text{\TeX}/\text{\LaTeX}$  file prepared by the author.